Conditioning Turbulent Channel Flows With Wall Plasma Jets

Conditioning turbulent channel flows with wall plasma jets

J. Seprieri *, G. Cafiero †, G. Iuso ‡
Department of Mechanical and Aerospace Engineering, Politecnico di Torino,
Corso Duca degli Abruzzi, 24, 10129, Turin, Italy

In this study, a fully developed turbulent channel flow is conditioned by an array of wall-mounted plasma actuators built to inject crosswise oscillating jets aiming at a control effect resembling the one caused with crosswise oscillations of the flow-exposed surfaces. Several oscillation frequencies were tested as well different duty cycles. Both these parameters can remarkably modify the flow forcing caused by the considered array of plasma actuators. The controlled flow was inspected with high-resolution PIV at two different wall normal planes, one near the wall and one within the log-layer. Statistical and instantaneous velocity-educed fields are discussed together with the statistical features of the low speed streaks. These are the velocity field footprint of drag-increasing flow structures typical of turbulent wall-bounded flows and, as such, their characteristics are interesting for friction drag reduction efforts.

Nomenclature

Re_τ	=	friction Reynolds number
u_τ	=	friction velocity [m/s]
h	=	channel height [m]
ν	=	kinematic viscosity [m^2/s]
x	=	streamwise direction [m]
y	=	wall normal direction [m]
z	=	crosswise direction [m]
u	=	streamwise velocity component [m/s]
v	=	wall normal velocity component [m/s]
w	=	crosswise velocity component [m/s]
U, V, W	=	time-averaged velocity component [m/s]
u', v', w'	=	time-fluctuations velocity component [m/s]
t	=	time [s]
f_{AC}	=	plasma actuators carrier frequency [Hz]
V_{pp}	=	plasma actuators peak-to-peak input-signal voltage [kV]
T	=	period of the plasma jets' modulation cycle [s]
DC	=	plasma jets' duty cycle
λ_z	=	plasma actuators' crosswise spacing [m]
ω	=	vorticity [1/s]
L	=	length [m]
W	=	width [m]
z_c	=	velocity streaks' center crosswise position [m]
$.^+$	=	quantity made non-dimensional with wall units
DBD	=	dielectric barrier discharge
PA	=	plasma actuators
PIV	=	particle image velocimetry
HV	=	high voltage
LSS	=	low speed streaks
pdf	=	probability density function

*Assistant professor, corresponding author: Jacopo.Serpieri@me.com
†Associate professor
‡Professor

s	=	velocity streaks
$\cdot_\alpha$	=	quantity referred to the α quantity, entity, or direction
$\bar{\cdot}$	=	time-averaged quantity

I. Introduction

Friction drag is the major contributor to the overall drag that an airliner needs to overcome during the cruise phase. Therefore, already a 1 % of drag reduction yields a reduction of about 0.75 % in burnt fuel. This translates to 10 million tonnes per year of saved CO2 emissions for the whole civilian aviation [1]. Passive techniques have been much explored given their easier deployment [2]. Nevertheless, the maximum power saving they can cater for caps to 10 % of the unforced flow drag, values achieved only in laboratory setups. On the other hand, active techniques can deliver drag reduction levels overcoming the value of 30 %. Against this approach, though, several factors play their game. These active flow control devices consume power to be operated, they usually are rather cumbersome embodiments and might have limited flow control authority due to technological limitations [2].

An active mean to reduce friction drag consists in inducing a layer of flow oscillating along the cross/spanwise direction thus behaving as a Stokes second problem flow [3]. The oscillating flow can disrupt the coherent structures present in turbulent wall-bounded flows and, therefore, reduce the transport of high-momentum fluid towards the wall [4, 5]. The latter is a major contribution to higher friction events and thus to friction drag. This forcing strategy has consequently gathered notable interest throughout the world (e.g. [6–11]). A further evolution of this flow control approach considers oscillating wall segments along the cross/spanwise but modulating these motions with waves traveling along the streamwise direction (e.g. [12–14]). This approach showed even larger levels of drag reduction while further complicating the possible implementation in real world applications.

In recent efforts, plasma actuators (PAs) have been considered as plausible flow actuators to induce a Stokes-like wall flow, similar to what caused by oscillating the flow-exposed surfaces along the crosswise direction, and capable of reducing the friction drag exerted by turbulent flows (e.g. [15–21]). The interest they collected is motivated by their simpler embodiment compared to mechanical, pneumatic or piezo-electric devices (e.g. [10, 14, 22, 23]). Nevertheless, the flow control effect that they induce differs from the more studied and understood strategies based on displacing the flow exposed surfaces and deserves more investigations. This study is motivated by this need.

II. Experimental setup

A. Flow facility and definitions

The experimental campaign took place in a channel flow facility (0.42 m x 0.035 m x 10 m, in width, height h and length), operated at the friction Reynolds number of $Re_\tau = \frac{u_\tau h/2}{\nu} = 190$ (where u_τ is the friction velocity and ν the kinematic viscosity).

A schematic of the setup exploited in this research is shown in Figure 1, which shows a side view of a portion of the flow facility, further showing some of the flow control and diagnostics equipment, discussed in detail below.

The coordinates system, also presented in Figure 1, used in this study consists of: x: the streamwise direction, y: the wall normal, and z: the crosswise directions, respectively. x originates at the actuator upstream edge, y at the wall and z at the channel spanwise center-line. The velocity components along these directions are denoted with u, v, w, respectively. Reynolds' decomposition will be considered: $[u(t), v(t), w(t)] = [U, V, W] + [u'(t), v'(t), w'(t)]$, where t is time and upper case letters and overlines, in the remainder, imply time-averages.

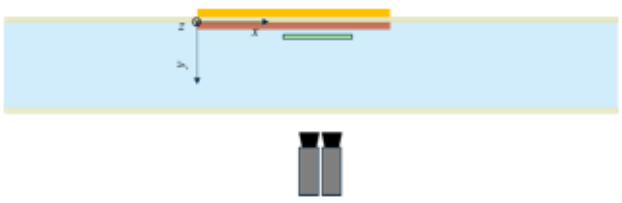

Fig. 1 Schematics side view of the PIV setup (not to scale): channel and actuators shown as in figure 2, laser plane (light green) and cameras (grey shapes).

B. Flow control

The flow actuator hereby considered featured an array of six dielectric barrier discharge (DBD) PAs with the electrodes aligned with and extending 600 mm along the streamwise direction. The PAs featured 0.5 mm thick polyethylene terephthalate sheets as the dielectric layer. The electrodes were made with 0.35 mm thick copper tape and the isolation of the encapsulated electrodes was guaranteed by multiple layers of *Kapton* tape. Every actuator featured one exposed electrode connected to the ground and two encapsulated electrodes, one per side of the exposed electrode, each connected to a high voltage (HV) source. The latter were four *GBS Elektronik Minipuls 4* set to deliver a sinusoidal signal of frequency $f_{AC} = 7$ kHz and peak-to-peak amplitude $V_{pp} = 8$ kV. A schematic of the actuator installed in the channel is shown in Figure 2.

According to the chosen actuation strategy, the HV signals were opportunely modulated. A schematic of the voltage-modulation effect can be extracted from Figure 2. For the considered actuation strategy, aiming at replicating the oscillating wall forcing, either the yellow or blue actuators were operated at the same instant and each set was operated for a given duty/modulation cycle DC. When for example a DC = 50 % was chosen, either the yellow or blue colored plasma discharges took place. When instead a larger DC (DC = 75 %) was set, there was a 25 % portion of the modulation period T when both the yellow and blue electrodes received a HV signal. Oppositely, when a smaller DC (DC = 25 %) was set, no HV signals arrived to both active electrode sets for 25 % T.

The modulation frequency was set to meet the literature-deemed-optimal non-dimensional period of $T^+ = 100$ (where the + labeled quantities are non-dimensionalised with inner-layer scales) (see [2, 3]). Furthermore, different periods were tested too. Namely, $T^+ = 16$, investigated by [16], but also $T^+ = 50$, and $T^+ = 150$ were considered.

The crosswise spacing of the actuators was set to $\lambda_z = 20$ mm corresponding to $\lambda_z^+ = 207.30$; i.e. about twice the average streaks' spacing).

The corresponding evolution of the induced plasma jets with the varying modulation period, duty cycle and crosswise spacing is not a trivial matter to assess. A dedicated thorough study on these aspects was carried out by [24]. In fact, depending also on the crosswise spacing between the oppositely-directed jets, setting different DC and T can lead to very different scenarios. For small modulation periods, the jets do not have the time to much propagate along the crosswise direction and might eventually collide with the incoming jets generated from the oppositely-lain electrode set. In this case, instead of the Stokes-like flow layer at the wall, wall-normal directed jets will take place roughly in the middle crosswise position between the oppositely-blowing actuators. This leads to a different forcing scenario which also proved effective in disrupting the flow coherent structures and reducing the friction drag (see [22, 25–28]). This forcing case is schematically shown in Figure 2 with the magenta arrows indicating the resulting upwelling fluid motions.

Clearly this is more likely to occur for smaller crosswise distances and for larger DCs. On the other side, longer modulation periods, larger crosswise distances between the PAs and smaller DCs can achieve the opposite effect where the jets evolve too far or for too long with this leading to an enhanced crosswise in-homogeneity of the induced control flow.

The flow forcing parameters define the flow cases considered in this study. The case name consists of the T^+ value followed by the DC value; for example the case 16 – 50 % features $T^+ = 16$ and DC = 50 %. The considered flow forcing cases are summarized in Table 1.

Table 1 Flow forced cases.

Case	V_{pp} [kV]	f_{AC} [kHz]	T^+	λ_z^+	DC [%]
16 – 50 %	8	7	16	207.30	50
50 – 50 %	8	7	50	207.30	50
100 – 50 %	8	7	100	207.30	50
150 – 50 %	8	7	150	207.30	50
16 – 25 %	8	7	100	207.30	25
16 – 75 %	8	7	100	207.30	75

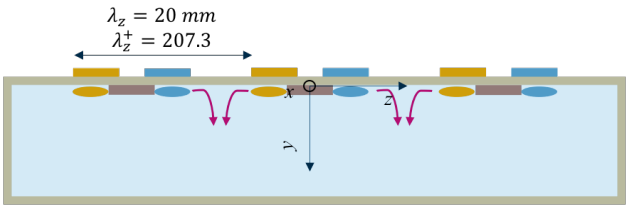

Fig. 2 Schematics of the setup as seen in a crossflow plane (not to scale): actuators spacing (λ_z, λ_z^+), operated electrodes (yellow and blue rectangles), exposed electrodes (brown rectangles), plasma discharges (oval shapes colored as the related HV electrodes), colliding plasma jets (magenta arrows).

C. Flow diagnostics

To inspect the effect of the performed flow actuation, a high-resolution planar PIV setup was arranged to have the measurement region aligned with the xz plane (see figure 1), at fixed wall normal positions. Two *Andor Zyla* sCMOS cameras (5.5 Mpx, 16 bits) and a *Litron* double cavity laser (200 mJ/pulse, 15 Hz maximum repetition rate) were deployed and installed as shown in figure 1. The cameras were equipped with *Tokina* 100 mm macro lens with green filters. The system synchronization was guaranteed by a *National Instrument PCI-6602* board. The acquisition frequency was 15 Hz and a total of 1000 image pairs per dataset was acquired.

The two cameras were placed one next to the other along the streamwise direction such to image a total field of view (FOV) extending 111.90 mm x 48.10 mm along the $x - z$ directions. This corresponds, in non-dimensional units, to 1550 x 497.40 along $x^+ - z^+$. The illuminated plane was set at $y = 5$ mm ($y^+ = 52$) and at $y = 10$ mm ($y^+ = 104$). The thickness of the laser sheet was set to ≈ 0.5 mm using light knives.

The proper orthogonal decomposition approach proposed by [29], was used to pre-process the PIV images to improve the particles signal and mitigate the effect of the laser reflections. A correlation-based multi-pass algorithm was then used to process the images. A spline interpolation of the images and the velocity fields was performed, as recommended by [30, 31] and a Blackmann weighting function was used to enhance the spatial resolution [32]. The final velocimetry resolution was 3.67 vectors/mm, i.e. 0.35 vectors per viscous length scale.

III. Results and discussion

A. Reference flow

The naturally evolving flow, considered here as a reference, is presented in this section. The streamwise, time averaged velocity U fields, measured at the two different wall-normal positions, are shown in Figures 3a ($y^+ = 52$) and 4a ($y^+ = 104$). Both fields show a good degree of uniformity thus suggesting that no appreciable angles between the laser sheet at the channel $x - z$ plane were present.

The plane measured component of the Reynolds stress tensor $\overline{u'w'}^+$ is also reported; see Figures 3b ($y^+ = 52$) and 4b ($y^+ = 104$). While the fields do show traces of $\overline{u'w'}^+$ regions, the values that are reported in the figures are small.

Finally, it is interesting to inspect a realization of the instantaneous streamwise velocity u' field. These fields are reported in Figures 3c ($y^+ = 52$) and 4c ($y^+ = 104$). While closer to the wall, streamwise- and crosswise- coherent regions of lower velocity, referred to as Low Speed Streaks (LSS), are clearly visible, in the logarithmic layer, these are larger in both directions but also less coherent.

In a related study, [33] showed stereo-PIV measurements of wall-normal-crosswise planes for the same dataset. The normalized timewise- and crosswise- averaged velocity profiles convincingly followed the canonical behaviour reported by [34, 35], thus indicating both the turbulent status of the measured flow and the reliability of the measurements.

B. Plasma-jets controlled flow

We move now to the inspection of the plasma-modified flow-fields. Starting from the U fields for the different forcing scenarios that are shown in Figure 5 for the $y^+ = 52$ measurements and in Figure 6 for the log-layer plane. The first evident aspect is that all the reported fields now feature a strong modulation along the crosswise direction when compared to the unforced flow-fields previously commented upon. These bands feature low velocity values in the

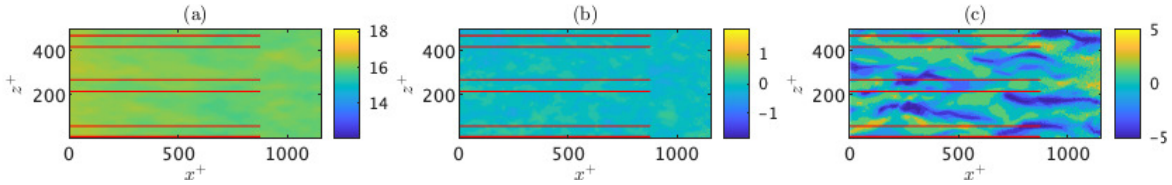

Fig. 3 U^+ **(a),** $\overline{u'w'}^+$ **(b) and** u' **fields for the reference flow at** $y = 5$ **mm** ($y^+ = 52$)**; PAs' exposed electrodes also shown (red lines).**

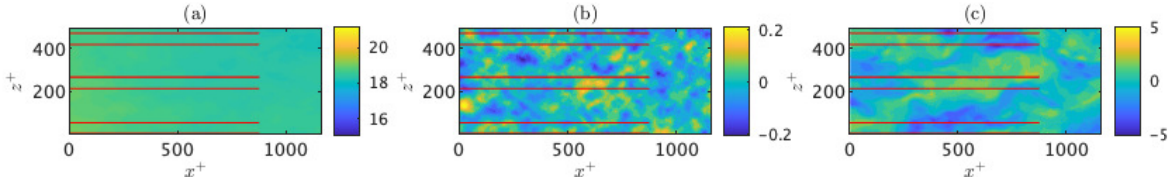

Fig. 4 U^+ **(a),** $\overline{u'w'}^+$ **(b) and** u' **fields for the reference flow at** $y = 10$ **mm** ($y^+ = 104$)**; PAs' exposed electrodes also shown (red lines).**

regions between the exposed electrodes. It can also be appreciated the effect of the finite extension of the actuators. In fact, at the downstream region of the measured fields, past the actuators, this modulation begins to fade away.

We can now focus on the effect of the modulation period. Going from the smallest T^+ to the largest (16, 50, 100, 150), it appears that the low-speed bands become broader and attain to milder values. This can be explained by the mechanisms discussed before: increasing the modulation period, the intensity of the upwelling motions of wall fluid, caused by the collision of the oppositely-directed jets, become weaker [24].

Inspecting instead the effect of the duty cycle, we can see that, while the DC = 50 % and DC= 75 % lead to rather similar time-averaged streamwise velocity fields, the DC = 25 % forcing seems to have a weaker velocity-modulating effect. The reason of this behavior shall require further analyses.

The focus now shall shift to the $\overline{u'w'}^+$ fields. These are shown in Figures 7 for the $y^+ = 52$ plane and to 8 for the log-layer measurement. As for the velocity fields, these Reynolds-stress component fields feature very strong crosswise modulations with aligned regions of positive and negative $\overline{u'w'}^+$ comprised between the exposed electrodes. For the $y^+ = 52$ measurement, going from smaller to larger values of T^+ makes these bands more pronounced. This suggests that lower frequency motions are, in average, more effective in enhancing the $u'w'$ motions. For the log-layer plane, it rather seems that the smaller and the larger modulation periods have stronger modulation effects.

For what concerns with the effect of the modulation cycle, for the $y^+ = 52$ plane, it can be said again that the DC = 50 % and DC = 75 % flow fields appear more similar to each other while the DC = 25 % case has milder regions of positive and negative $\overline{u'w'}^+$. The opposite seems instead to be true for the $y^+ = 105$ plane, where the DC = 25 % case is showing slightly more pronounced bands.

We consider now, as done before for the unforced flow, the effect of the different forcing on the instantaneous streamwise velocity u'. In Figures 9 and 10, these fields are shown for the $y^+ = 52$ and $y^+ = 104$ planes, respectively. Although inferring meaningful information from instantaneous realizations of chaotic phenomena is a naive attempt and statistical analyses are required, the inspection of these fields can still give some interesting insights. Besides, the next section will present more suited statistical analyses.

Starting as done so far with the effect of the modulation period, it appears that increasing T^+, the spatial coherence of the measured low speed regions reduces. With respect to the DC effect, again it seems that DC = 25 % sets itself more apart compared to the other two considered cases.

An interesting visual feature that can be inferred from the presented plots, is the tendency of the shown coherent low speed regions to arrange themselves along a wavy pattern although of different wavelength among the different forcing parameters, as a consequence of the performed actuation. This is particularly evident for the 100 – 25 % case at $y^+ = 52$ and for the 100 – 75 % case at $y^+ = 104$. Although, again, we shall point out that the more or less pronounced wavy shape of these regions might just be casually captured within the presented instantaneous fields.

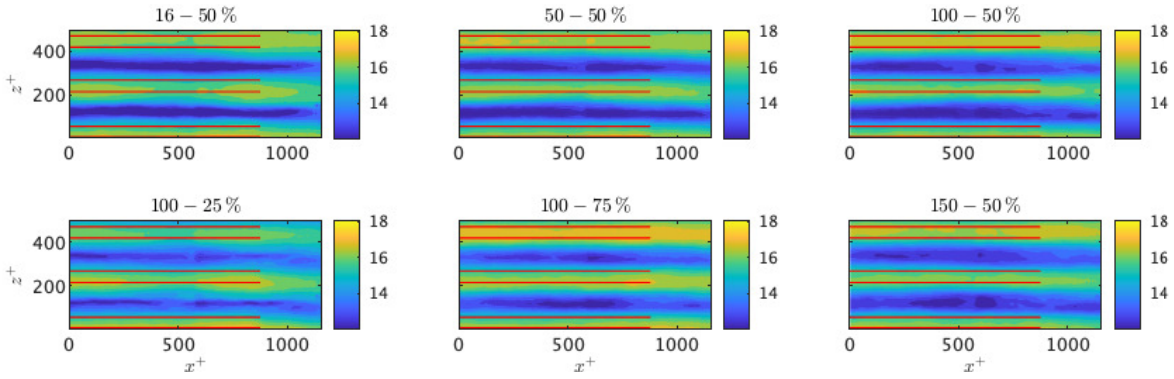

Fig. 5 U^+ fields for the plasma-jets controlled flows at $y = 5$ mm ($y^+ = 52$); PAs' exposed electrodes also shown (red lines).

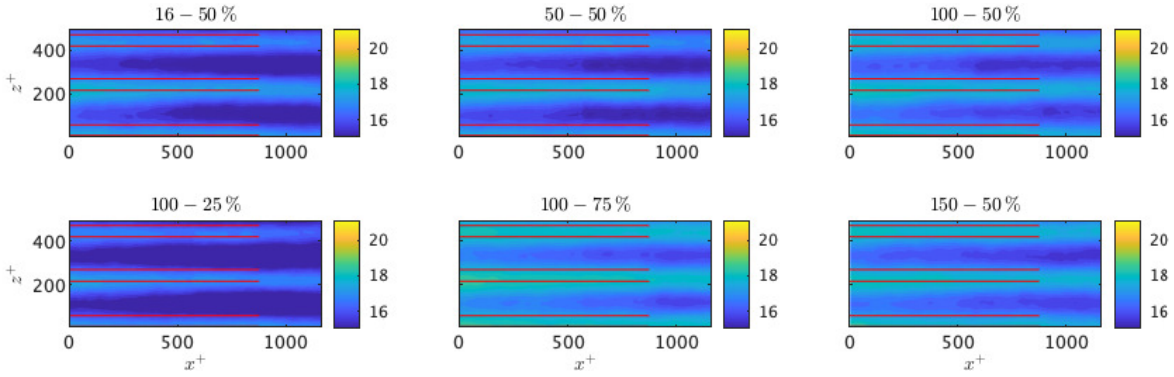

Fig. 6 U^+ fields for the plasma-jets controlled flows at $y = 10$ mm ($y^+ = 104$); PAs' exposed electrodes also shown (red lines).

C. Forcing effect on LSS properties

In this section, the LSS features are statistically analysed extracting connected regions of $u' < 0$, extending in the streamwise direction for at least 100 viscous length scales. The velocity fields are then conditionally averaged to derive LSS statistical features. This procedure follows the approach proposed by [22, 36]. The results of this analysis are shown in Figures 11 and 12 for the $y^+ = 52$ and the $y^+ = 104$ plane, respectively. Starting from the LSS-conditioned crosswise velocity u_s^+, within the $y^+ = 52$ plane, it appears that all the performed control strategies led to remarkable reductions of the velocity deficit measured for the unforced reference flow. In particular, the 100 – 25 % forcing considerably flattened the u_s^+ profile. Similarly, the wall-normal vorticity profiles appear much damped by the plasma jets. Moreover, and again in particular for the 100 – 25 % case, the distance between the profile positive and negative peaks is much reduced. Considering instead the probability density function (pdf), it can be seen that the LSS average streamwise length L_s^+ and crosswise width W_s^+ appear slightly increased by the performed forcing.

Within the buffer layer plane at $y^+ = 104$, the scenario considerably changes: the streamwise velocity profile deficit becomes more pronounced, compared to the unforced reference flow, for all the plasma-forced cases but the 100 – 25 % case. The vorticity profiles are more overlapping still considering the exception of the 100 – 25 % case. Finally, while the average streaks' width seems not substantially impacted by the plasma jets, the average length appears considerably reduced by the applied forcing.

IV. Concluding remarks

In this study, wall-mounted arrays of plasma actuators were considered as flow actuators to induce, in a fully developed turbulent channel flow, a flow forcing effect similar to the one achievable with oscillating the flow exposed surfaces along the crosswise direction.

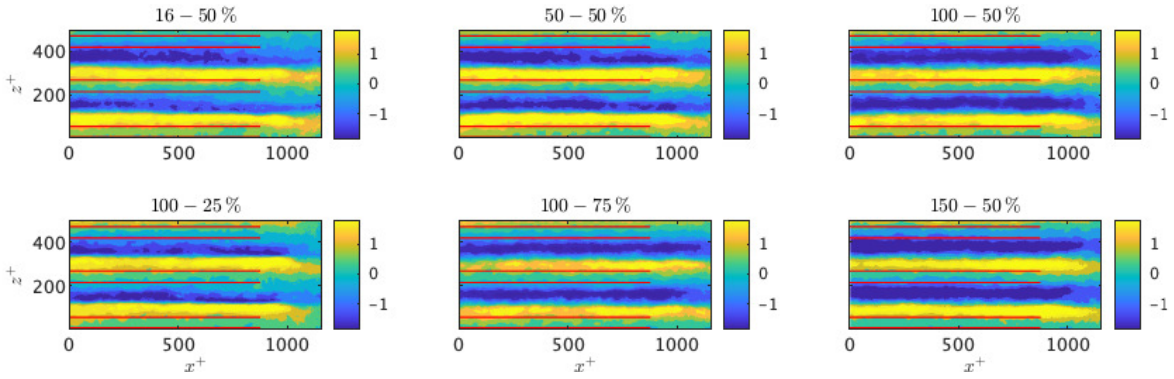

Fig. 7 $\overline{u'w'}^+$ fields for the plasma-jets controlled flows at $y = 5$ mm ($y^+ = 52$); PAs' exposed electrodes also shown (red lines).

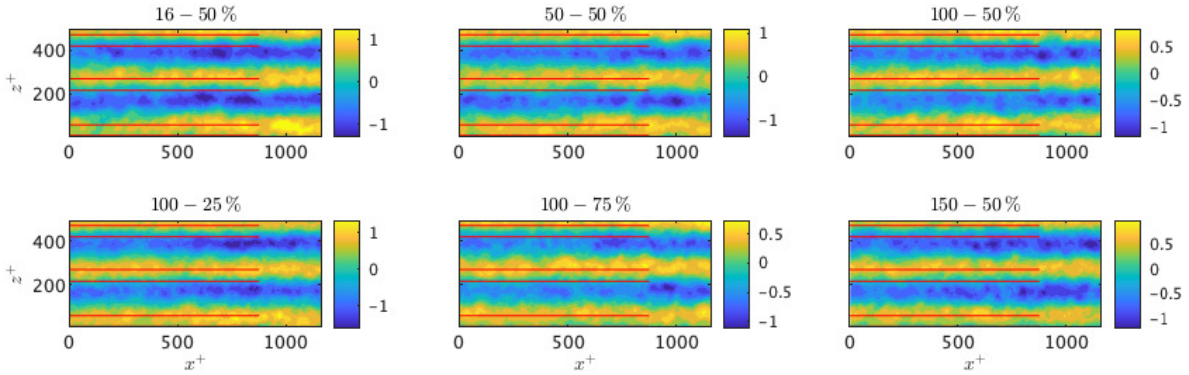

Fig. 8 $\overline{u'w'}^+$ fields for the plasma-jets controlled flows at $y = 10$ mm ($y^+ = 104$); PAs' exposed electrodes also shown (red lines).

The controlled flow fields were inspected with high resolution wall parallel PIV at two different wall normal planes: one within the wall region and one in the flow logarithmic layer.

The results hereby presented show strong effects from the performed actuation on the time-averaged, and instantaneous flow as well as on the coherent turbulent structures. Furthermore, these effects considerably varied with respect to the investigated flow control parameters.

Acknowledgements

This study was carried out within the "WAll-Turbulence Active COntrol" project – funded by European Union – Next Generation EU within the PRIN 2022 PNRR program (D.D.1409 del 14/09/2022 Ministero dell'Università e della Ricerca). This manuscript reflects only the authors' views and opinions and the Ministry cannot be considered responsible for them.

The authors are thankful to F. M. Ricci for considerably contributing to the experimental campaign.

References

[1] Ricco, P., Skote, M., and Leschziner, M. A., "A review of turbulent skin-friction drag reduction by near-wall transverse forcing," *Progress in Aerospace Sciences*, Vol. 123, 2021, p. 100713. https://doi.org/10.1016/J.PAEROSCI.2021.100713.

[2] Ghaemi, S., "Passive and active control of turbulent flows," *Physics of Fluids*, Vol. 32, No. 8, 2020. https://doi.org/10.1063/5.0022548.

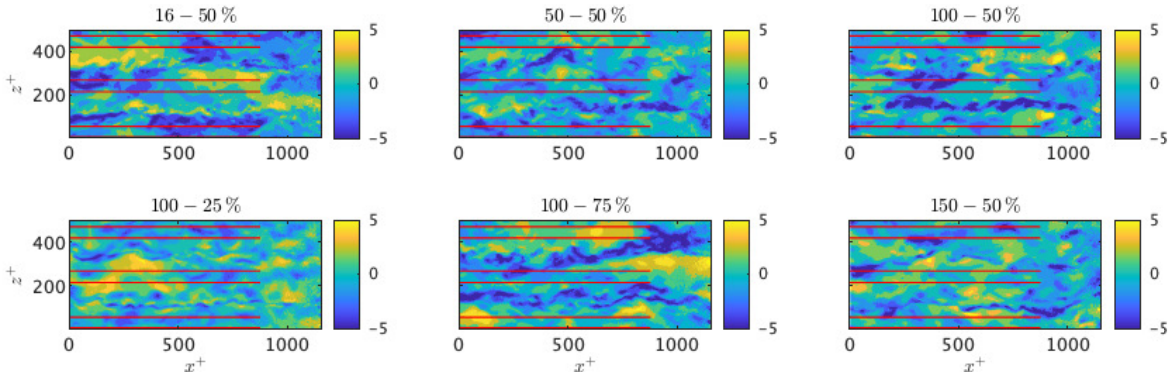

Fig. 9 u' **fields for the plasma-jets controlled flows at** $y = 5\,\mathbf{mm}$ **(**$y^+ = 52$**); PAs' exposed electrodes also shown (red lines).**

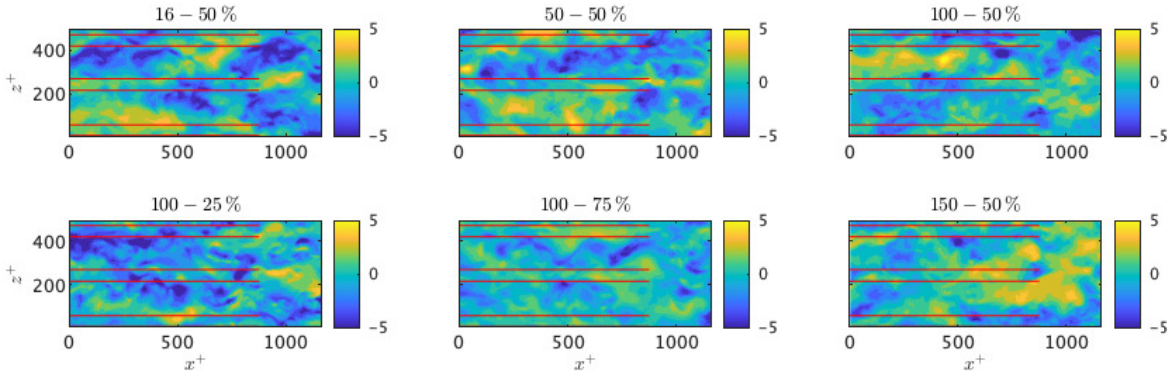

Fig. 10 u' **fields for the plasma-jets controlled flows at** $y = 10\,\mathbf{mm}$ **(**$y^+ = 104$**); PAs' exposed electrodes also shown (red lines).**

[3] Karniadakis, G. E., and Choi, K.-S., *Annual Review of Fluid Mechanics*, Vol. 35, 2003, pp. 45–62. https://doi.org/10.1146/annurev.fluid.35.101101.161213.

[4] Leschziner, M. A., "Friction-Drag Reduction by Transverse Wall Motion - A Review," *Journal of Mechanics*, Vol. 36, No. 5, 2020, pp. 649–663. https://doi.org/10.1017/jmech.2020.31.

[5] Choi, H., Moin, P., and Kim, J., "Active turbulence control for drag reduction in wall-bounded flows," *Journal of Fluid Mechanics*, Vol. 262, 1994, pp. 75–110. https://doi.org/10.1017/S0022112094000431.

[6] Akhavan, R., Jung, W. J., and Mangiavacchi, N., "Turbulence control in wall-bounded flows by spanwise oscillations," *Applied Scientific Research*, Vol. 51, 1993, pp. 299–303. https://doi.org/10.1007/BF01082552.

[7] Jung, W. J., Mangiavacchi, N., and Akhavan, R., "Suppression of turbulence in wall-bounded flows by high-frequency spanwise oscillations," *Physics of Fluids A*, Vol. 4, 1992, pp. 1605–1607. https://doi.org/10.1063/1.858381.

[8] Choi, K.-S., and Graham, M., "Drag reduction of turbulent pipe flows by circular-wall oscillation," *Physics of Fluids*, Vol. 10, No. 1, 1998, pp. 7–9. https://doi.org/10.1063/1.869538.

[9] Yuan, W., Zhang, M., Cui, Y., and Khoo, B. C., "Phase-space dynamics of near-wall streaks in wall-bounded turbulence with spanwise oscillation," *Physics of Fluids*, Vol. 31, 2019. https://doi.org/10.1063/1.5130161.

[10] Di Cicca, G. M., Iuso, G., Spazzini, P. G., and Onorato, M., "Particle image velocimetry investigation of a turbulent boundary layer manipulated by spanwise wall oscillations," *Journal of Fluid Mechanics*, 2002. https://doi.org/10.1017/S002211200200157X.

[11] Gatti, D., Güttler, A., Frohnapfel, B., and Tropea, C., *Experiments in Fluids*, Vol. 56, No. 5, 2015, p. 110. https://doi.org/10.1007/s00348-015-1983-x.

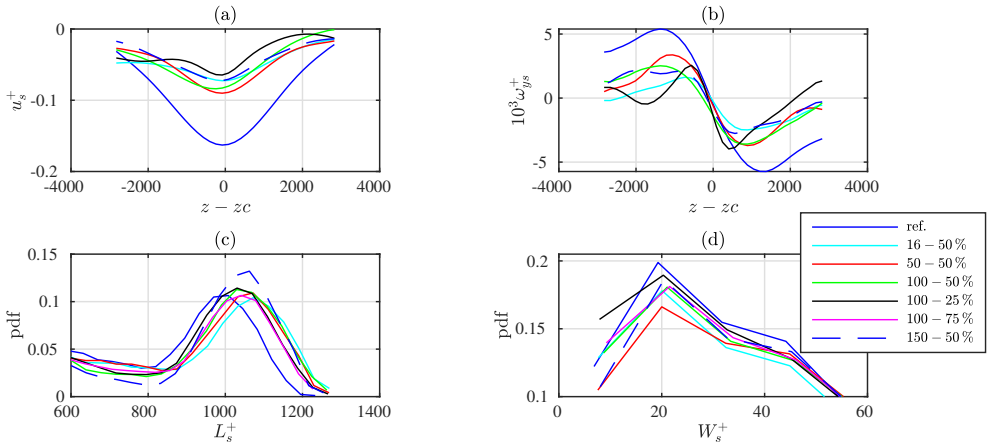

Fig. 11 LSS features, at the $y = 5$ mm ($y^+ = 52$) measurement plane: u_s^+ (a); $10^3\,\omega_{ys}^+$ (b); pdf of L_s^+ (c) and pdf of W_s^+ (d); z_c is the LSS center along z.

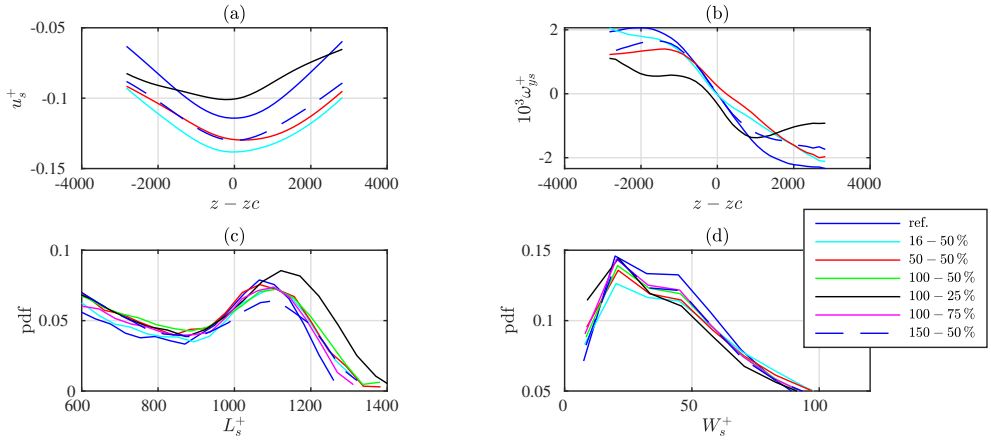

Fig. 12 LSS features, at the $y = 10$ mm ($y^+ = 104$) measurement plane: u_s^+ (a); $10^3\,\omega_{ys}^+$ (b); pdf of L_s^+ (c) and pdf of W_s^+ (d); z_c is the LSS center along z.

[12] Quadrio, M., Ricco, P., and Viotti, C., "Streamwise-travelling waves of spanwise wall velocity for turbulent drag reduction," *Journal of Fluid Mechanics*, Vol. 627, 2009, pp. 161–178. https://doi.org/10.1017/S0022112009006077.

[13] Gatti, D., and Quadrio, M., *Journal of Fluid Mechanics*, Vol. 802, 2016, pp. 553–582. https://doi.org/10.1017/jfm.2016.485.

[14] Marusic, I., Chandran, D., Rouhi, A., Fu, M. K., Wine, D., Holloway, B., Chung, D., and Smits, A. J., "An energy-efficient pathway to turbulent drag reduction," *Nature Communications*, Vol. 12, No. 1, 2021, pp. 1–8. https://doi.org/10.1038/s41467-021-26128-8.

[15] Choi, K.-S., Jukes, T., and Whalley, R., *Philosophical Transactions of the Royal Society A: Mathematical, Physical and Engineering Sciences*, Vol. 369, No. 1940, 2011, pp. 1443–1458. https://doi.org/10.1098/RSTA.2010.0362.

[16] Whalley, R. D., and Choi, K. S., "Turbulent boundary-layer control with plasma spanwise travelling waves," *Experiments in Fluids*, Vol. 55, No. 8, 2014. https://doi.org/10.1007/S00348-014-1796-3.

[17] Mahfoze, O., and Laizet, S., *International Journal of Heat and Fluid Flow*, Vol. 66, 2017, pp. 83–94. https://doi.org/10.1016/J.IJHEATFLUIDFLOW.2017.05.013.

[18] Hehner, M. T., Gatti, D., and Kriegseis, J., "Stokes-layer formation under absence of moving parts - A novel oscillatory plasma actuator design for turbulent drag reduction," *Physics of Fluids*, Vol. 31, No. 5, 2019, pp. 1–6. https://doi.org/10.1063/1.5094388.

[19] Thomas, F. O., Corke, T. C., Duong, A., Midya, S., and Yates, K., "Turbulent drag reduction using pulsed-DC plasma actuation," *Journal of Physics D: Applied Physics*, Vol. 52, 2019. https://doi.org/10.1088/1361-6463/ab3388.

[20] Hehner, M. T., Gatti, D., Mattern, P., Kotsonis, M., and Kriegseis, J., "Beat-frequency-operated dielectric barrier discharge plasma actuators for virtual wall oscillations," *AIAA Journal*, Vol. 59, No. 2, 2021, pp. 763–767. https://doi.org/10.2514/1.J059802.

[21] Serpieri, J., Hehner, M. T., and Kriegseis, J., "Steady Bi-dimensional Crossflow Plasma Jets in Turbulent Channel Flows," *Flow, Turbulence and Combustion*, 2023. https://doi.org/10.1007/s10494-023-00463-w.

[22] Iuso, G., and Di Cicca, G. M., "Interaction of synthetic jets with a fully developed turbulent channel flow," *Journal of Turbulence*, 2009. https://doi.org/10.1080/14685240601110088.

[23] Auteri, F., Baron, A., Belan, M., Campanardi, G., and Quadrio, M., *Physics of Fluids*, Vol. 22, No. 11, 2010. https://doi.org/10.1063/1.3491203.

[24] Zong, H., Su, Z., Liang, H., and Wu, Y., "Experimental investigation and reduced-order modeling of plasma jets in a turbulent boundary layer for skin-friction drag reduction," *Physics of Fluids*, Vol. 34, 2022. https://doi.org/10.1063/5.0104609.

[25] Schoppa, W., and Hussain, F., "A large-scale control strategy for drag reduction in turbulent boundary layers," *Physics of Fluids*, Vol. 10, 1998, pp. 1049–1051. https://doi.org/10.1063/1.869789.

[26] Yao, J., Chen, X., and Hussain, F., "Drag control in wall-bounded turbulent flows via spanwise opposed wall-jet forcing," *Journal of Fluid Mechanics*, Vol. 852, No. August, 2018, pp. 678–709. https://doi.org/10.1017/jfm.2018.553.

[27] Cannata, M., Cafiero, G., and Iuso, G., "Large-scale forcing of a turbulent channel flow through Spanwise synthetic jets," *AIAA Journal*, Vol. 58, 2020, pp. 2042–2052. https://doi.org/10.2514/1.J059047.

[28] Cheng, X. Q., Wong, C. W., Hussain, F., Schröder, W., and Zhou, Y., "Flat plate drag reduction using plasma-generated streamwise vortices," *Journal of Fluid Mechanics*, Vol. 918, 2021, pp. 1–37. https://doi.org/10.1017/jfm.2021.311.

[29] Mendez, M. A., Raiola, M., Masullo, A., Discetti, S., Ianiro, A., Theunissen, R., and Buchlin, J. M., "POD-based background removal for particle image velocimetry," *Experimental Thermal and Fluid Science*, Vol. 80, 2017, pp. 181–192. https://doi.org/10.1016/J.EXPTHERMFLUSCI.2016.08.021.

[30] Astarita, T., "Analysis of interpolation schemes for image deformation methods in PIV: Effect of noise on the accuracy and spatial resolution," *Experiments in Fluids*, Vol. 40, 2006, pp. 977–987. https://doi.org/10.1007/S00348-006-0139-4.

[31] Astarita, T., "Analysis of velocity interpolation schemes for image deformation methods in PIV," *Experiments in Fluids*, Vol. 45, 2008, pp. 257–266. https://doi.org/10.1007/S00348-008-0475-7.

[32] Astarita, T., "Analysis of weighting windows for image deformation methods in PIV," *Experiments in Fluids*, Vol. 43, 2007, pp. 859–872. https://doi.org/10.1007/S00348-007-0314-2.

[33] Ricci, F., Amico, E., Cafiero, G., Iuso, G., and Serpieri, J., *Progress in Turbulence X*, Springer Cham, 2024, Chaps. Crossflow-oscillating plasma jets in a turbulent channel flow.

[34] Pope, S. B., *Turbulent flows*, Cambridge University Press, 2000.

[35] Van Driest, E., "On turbulent flow near a wall," *Journal of the Aeronautical Sciences*, 1956. https://doi.org/doi:10.2514/8.3713.

[36] Cafiero, G., Amico, E., and Iuso, G., "Manipulation of a turbulent boundary layer using sinusoidal riblets," *Journal of Fluid Mechanics*, Vol. 984, 2024, p. A59. https://doi.org/10.1017/JFM.2024.256.